PROCEEDINGS OF SPIE

SPIEDigitalLibrary.org/conference-proceedings-of-spie

Vascular elastic photoacoustic tomography in humans

Pengfei Hai, Yong Zhou, Jinyang Liang, Chiye Li, Lihong V. Wang

Pengfei Hai, Yong Zhou, Jinyang Liang, Chiye Li, Lihong V. Wang, "Vascular elastic photoacoustic tomography in humans," Proc. SPIE 9708, Photons Plus Ultrasound: Imaging and Sensing 2016, 970803 (15 March 2016); doi: 10.1117/12.2219700

SPIE.

Event: SPIE BiOS, 2016, San Francisco, California, United States

Downloaded From: https://www.spiedigitallibrary.org/conference-proceedings-of-spie on 9/4/2018 Terms of Use: https://www.spiedigitallibrary.org/terms-of-use

Vascular elastic photoacoustic tomography in humans

Pengfei Hai, Yong Zhou, Jinyang Liang, Chiye Li, and Lihong V. Wang*

Optical Imaging Laboratory, Department of Biomedical Engineering, Washington University in St. Louis, One Brookings Drive, St. Louis, Missouri 63130

*Corresponding author: lhwang@biomed.wustl.edu

ABSTRACT

Quantification of vascular elasticity can help detect thrombosis and prevent life-threatening conditions such as acute myocardial infarction or stroke. Here, we propose vascular elastic photoacoustic tomography (VE-PAT) to measure vascular elasticity in humans. VE-PAT was developed by incorporating a linear-array-based photoacoustic computed tomography system with a customized compression stage. By measuring the deformation of blood vessels under uniaxial loading, VE-PAT was able to quantify the vascular compliance. We first demonstrated the feasibility of VE-PAT in blood vessel phantoms. In large vessel phantoms, VE-PAT detected a decrease in vascular compliance due to simulated thrombosis, which was validated by a standard compression test. In small blood vessel phantoms embedded 3 mm deep in gelatin, VE-PAT detected elasticity changes at depths that are difficult to image using other elasticity imaging techniques. We then applied VE-PAT to assess vascular compliance in a human subject and detected a decrease in vascular compliance when an occlusion occurred downstream from the measurement point, demonstrating the potential of VE-PAT in clinical applications such as detection of deep venous thrombosis.

Keywords: photoacoustic tomography, vascular elastography, vascular elasticity, thrombosis

1. INTRODUCTION

Elastic properties of biological tissue are often altered in pathological states[1,2]. Detecting such alterations has become an important tool in clinical diagnosis for doctors and physicians. In blood vessels, the elastic properties are strongly affected by abnormal hemodynamic states induced by thrombosis, which can lead to severe conditions such as acute myocardial infarction, stroke, and pulmonary embolism[3,4]. Thus, quantification of vascular elastic properties can contribute to the detection of thrombosis and prevention of potential life threatening conditions.

Elastography, inspired by manual palpation, is a medical imaging technique that maps tissue elasticity[5]. Elastography has been achieved using several imaging modalities including ultrasound elastography (USE)[6], magnetic resonance elastography (MRE)[7], optical coherence elastography (OCE)[8], and photoacoustic elastography (PAE)[9]. Elastography has been applied for blood vessel stiffness characterization, termed as vascular elastography[10]. An invasive method using endovascular imaging catheters was first implemented to perform vascular elastography[11]. Vascular elastography was then achieved using USE, MRE, and OCE[12-14]. However, each of them suffers certain limitations. USE can image blood vessels in deep regions, but the poor ultrasonic scattering contrast between blood and extravascular tissue makes it insensitive to the deformations of small blood vessels. MRE can potentially penetrate the whole human body, but its spatial resolution (~1 to 3 mm) is sufficient for assessing the stiffness of large blood vessels only. Benefiting from the high spatial resolution of optical coherence tomography, OCE has a typical spatial resolution of 1 to 10 μm and can detect displacement at the submicrometer level. Thus it is capable of mapping small blood vessel elasticity. However, OCE suffers from strong optical scattering in biological tissue, limiting its penetration depth to ~1 mm, which is insufficient for assessing elastic properties of blood vessels in the optical diffusive regime in tissues.

By ultrasonically detecting optical absorption, photoacoustic tomography (PAT) achieves high spatial resolution at depths beyond the optical diffusion limit[15]. With high sensitivity for vasculature imaging thanks to the strong optical absorption contrast provided by hemoglobin in red blood cells, PAT has proven capable of providing structural, functional, and mechanical properties of blood vessels in both animal models and humans[16-19]. PAT has also been applied to measure the elastic properties of biological tissue. However, the existing technique is not applicable for assessing the vascular elastic properties in humans[20].

Photons Plus Ultrasound: Imaging and Sensing 2016, edited by Alexander A. Oraevsky, Lihong V. Wang
Proc. of SPIE Vol. 9708, 970803 · © 2016 SPIE · CCC code: 1605-7422/16/$18 · doi: 10.1117/12.2219700

Downloaded From: https://www.spiedigitallibrary.org/conference-proceedings-of-spie on 9/4/2018
Terms of Use: https://www.spiedigitallibrary.org/terms-of-use

Here, we report vascular elastic photoacoustic tomography (VE-PAT), capable of measuring vascular elastic properties in the optical diffusive regime in humans. We first demonstrated the feasibility of VE-PAT by measuring vascular compliance changes in both large and small blood vessel phantoms at depths due to simulated thrombosis. We further applied this technique to humans and detected a decrease of blood vessel compliance after downstream vessel occlusion, demonstrating the potential of VE-PAT in clinical thrombosis detection.

2. MATERIALS AND METHODS

2.1 Experimental system

In VE-PAT, the major device is a linear-array-based photoacoustic imaging probe[21,22]. The probe used here consisted of a linear array ultrasonic transducer (Visualsonics Inc. LZ250, 21 MHz center frequency, 78% one-way bandwidth, 256 elements, 23 × 3 mm array size) with two optical fiber bundle strips (20 × 1.25 mm) mounted on each side [Fig. 1(a)]. The laser beams coming out of the two optical fiber bundle strips had an angle of incidence of 30 deg with respect to the imaging plane. The two optical fiber bundles were bifurcated from a single optical bundle that was incorporated into the probe together with an ultrasound signal cable. A tunable optical parametric oscillator laser (680 to 970 nm, 20-Hz pulse repetition rate) was coupled into the single fiber optical bundle for photoacoustic excitation. The wavelength was set to 850 nm to achieve deep penetration for vascular elasticity imaging. In our experiments, the fluence on the sample surface was 10 mJ/cm^2, well within the safety limit set by the American National Standards Institute (20 mJ/cm^2). Each element of the transducer array was cylindrically focused with a focal length of 15 mm. For each of four laser pulses, photoacoustic signals were captured sequentially on one quarter (i.e., 64 elements) of the transducer array elements. After all data were acquired from the four segments, we reconstructed a two-dimensional (2-D) photoacoustic image using the filtered back-projection algorithm[23]. The reconstructed 2-D photoacoustic image is referred to hereafter as the B-scan photoacoustic image. An imaging station (Vevo LAZR, Visualsonics Inc.) displayed the reconstructed B-scan photoacoustic images at 5 frames/s, as determined by the 20 Hz laser repetition rate and the four-to-one multiplexing in the image acquisition system. The VE-PAT system has spatial resolutions of 119 μm in the lateral direction, 86 μm in the axial direction, and 1237 μm in the elevational direction. The minimum displacement that can be resolved is 18.3 μm, which is determined by the data acquisition sampling rate of 84 MHz and the average speed of sound in biological tissue of 1540 m/s.

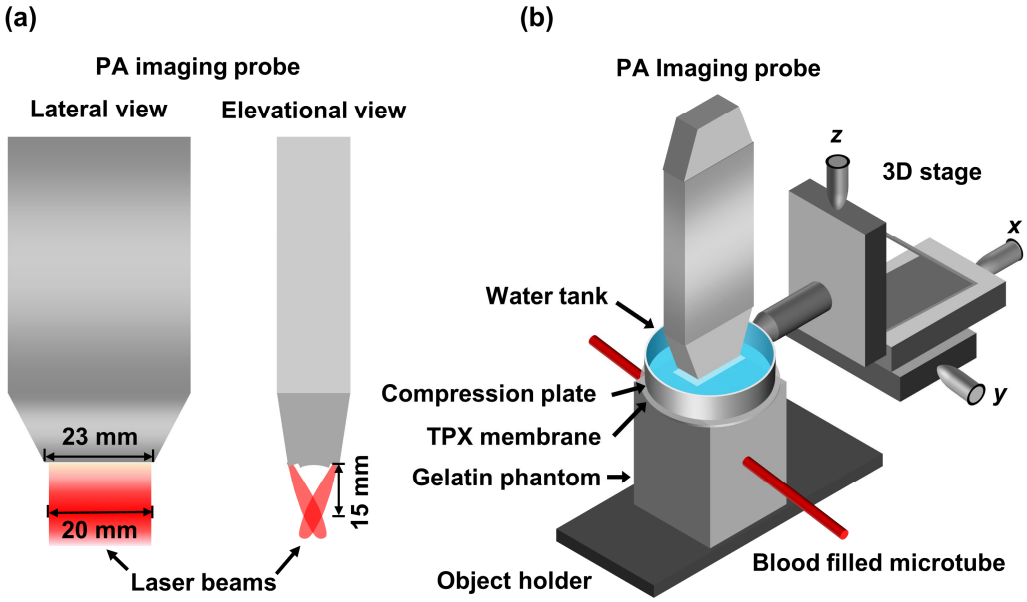

Figure 1. Schematic of vascular elastic photoacoustic tomography (VE-PAT): (a) photoacoustic imaging probe and (b) VE-PAT setup for a blood vessel phantom imaging. The imaging probe is incorporated with a customized compression stage.

Downloaded From: https://www.spiedigitallibrary.org/conference-proceedings-of-spie on 9/4/2018
Terms of Use: https://www.spiedigitallibrary.org/terms-of-use

To implement VE-PAT, a customized compression stage was developed and incorporated into the probe. The compression stage had an aluminum plate controlled by a three-dimensional translation stage, which could position the plate in the x-y plane and induce precise displacements along the z axis for accurate sample compression [Fig. 1(b)]. Above the compression plate, a water tank held water for acoustic coupling. An imaging window slightly larger than the probe was machined in the center of the compression plate. To ensure the compression force applied to the sample was normal and uniaxial, a piece of fully stretched polymethylpentene plastic membrane was attached to the bottom of the compression plate, which allowed the transmission of both the optical excitation light and the generated photoacoustic wave. An aluminum block on an optical table held the sample against compression.

2.2 Phantom preparation

Silicone microtubes with 0.3 mm (60985-700, VWR) and 3.4 mm inner diameters (IDs) (60985-720, VWR) perfused with bovine blood (905, Quad-Five) mimicked small and large blood vessels, respectively. Blood was pumped into the microtubes through a syringe, and the flow speed was controlled by a syringe pump (BSP-99M, Braintree Scientific). The thrombosis was simulated by injecting a small drop of glue into the microtube downstream from the measurement point, which hardened on the tube wall and partially blocked the flow. The microtube was then embedded in tissue-mimicking gelatin phantoms 3 mm deep [Fig. 2(a)]. To achieve stiffness similar to that of soft tissue, the gelatin concentration in the phantoms was 100 g/L[24]. To achieve similar optical scattering as in biological tissue, 1% intralipid was added to the gelatin phantoms.

2.3 Methods

2.3.1 Sample compression and photoacoustic image acquisition

Elastic property changes induced by simulated thrombosis were investigated in both the large and small blood vessel phantoms. As shown in Fig. 1(b), the axis of the phantom blood vessel was perpendicular to the imaging plane. A cross section of the phantom was first imaged right after the compression plate contacted the sample with a minimum load. For the big vessel (ID = 3.4 mm), we applied 10 small steps of compression with a step size of 50 μm and two large steps of compression with a step size of 500 μm. For the small vessel phantom (ID = 0.3 mm), only one 50 μm step compression was applied instead of 12 steps. For all the compression steps, corresponding photoacoustic images were acquired when the phantom had stabilized. The same compression and imaging procedure was performed in both conditions, with and without simulated thrombosis.

In vivo blood vessel elasticity was assessed on the middle finger of the right hand of a 29-year-old male volunteer. All of the experiments were conducted in accordance with the human studies protocols approved by the Institutional Review Board at Washington University in St. Louis. The right hand was placed on the object holder, and the middle finger was fixed in position and imaged by the VE-PAT system. Similar to the procedures in our phantom experiments, a cross section of the finger was first imaged just after the compression plate contacted the finger with a minimum load. Then we applied five small steps of compression with a step size of 50 μm and two large steps of compression with a step size of 300 μm. Photoacoustic images were acquired after each step of compression. To simulate thrombosis, a vessel occlusion was created on the near end of the middle finger. The same compression and imaging procedure were repeated to obtain the elastic property changes of a finger vessel due to the occlusion. The occlusion time was short enough (60 s) to avoid any potential harm.

2.3.2 Strain calculation

Strain values of the blood vessel phantoms and the finger blood vessels under compression were obtained via analyzing the reconstructed B-scan photoacoustic images before and after compression based on the following method. First, the photoacoustic images at preload were segmented based on a threshold of 6 dB with respect to the noise level, and the original distances L between the top and bottom boundaries of the blood vessels were calculated at each reconstructed A-line. Then, corresponding reconstructed A-lines in the photoacoustic images before and after compression were analyzed with a sliding window cross-correlation method[25]. The sliding window was set slightly larger than the visible vessel boundaries in the photoacoustic images. By doing cross correlation between the corresponding signals within the window before and after compression, axial displacements of the top and bottom boundaries, denoted as d_t and d_b, were estimated. The strain ε was then calculated by

$$\varepsilon = \frac{d_t - d_b}{L}. \quad (1)$$

Downloaded From: https://www.spiedigitallibrary.org/conference-proceedings-of-spie on 9/4/2018
Terms of Use: https://www.spiedigitallibrary.org/terms-of-use

As the compliance C is proportional to the strain ε, the ratio of the compliances C_1 and C_2 of two samples under the same stress equals the ratio of their strains ε_1 and ε_2:

$$\frac{C_1}{C_2} = \frac{\varepsilon_1}{\varepsilon_2}. \tag{2}$$

3. RESULTS

3.1 Standard compression test of the large blood vessel phantom

Before the microtubes were embedded into tissue-mimicking gelatin phantoms, the compliances of the perfused large blood vessel phantoms with and without simulated thrombosis were measured with a standard compression test. In the standard compression test, the large blood vessel phantom was placed on a high-precision digital weighing scale (S200, Ohaus) and compressed using the customized compression stage. The compression stress was calculated based on the difference in the scale readings before and after compression. The axial displacement of the top boundary was read from the translation stage that moved the compression plate along the z axis for precise sample compression. Because the bottom boundary did not move, the strain was calculated as the deformation over the original diameter of the blood vessel phantom [Eq. (1)]. Consistent with the previous elasticity imaging studies[26], the strain–stress relationship appeared linear with the coefficient of determination (R^2) of 0.993 and 0.987 when the strain was smaller than 10% [Fig. 2(b)]. The ratio of the compliances between cases with and without simulated thrombosis was 0.64.

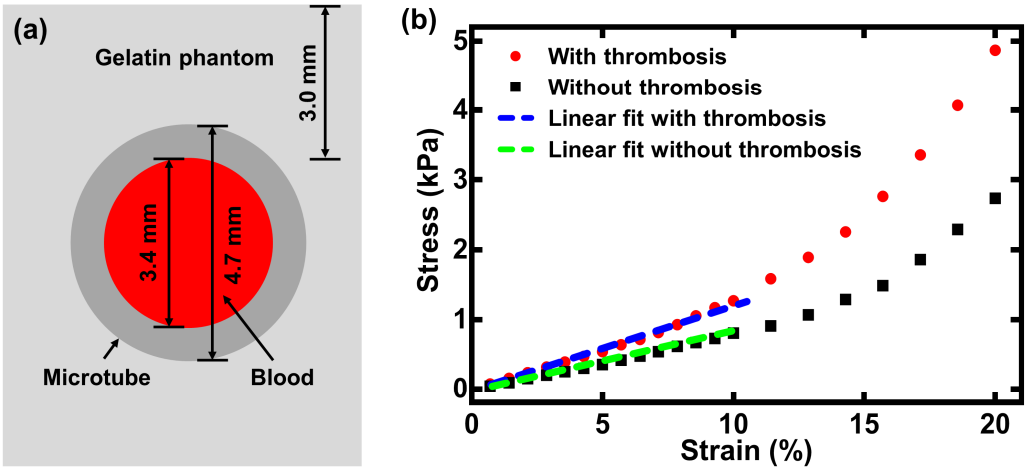

Figure 2. Characterization of a large blood vessel phantom: (a) diagram of the large blood vessel phantom embedded 3 mm deep in gelatin and (b) stress-strain response measured for the large blood vessel phantom with and without simulated thrombosis. Stress–strain curves with strain smaller than 10% were fitted to linear functions to calculate the compliances as shown by the dashed lines.

3.2 Vascular elastic photoacoustic tomography of large blood vessel phantom

Photoacoustic images of a cross section of the large blood vessel phantom before and after 10 small steps of compression with a step size of 50 μm are shown in Fig. 3. Under the same stress, the blood vessel phantom without simulated thrombosis [Figs. 3(a) and 3(b)] underwent larger deformation than that with simulated thrombosis [Figs. 3(c) and 3(d)]. The strain values of the large blood vessel phantom with and without simulated thrombosis were plotted at each compression step [Fig. 3(e)]. During the 10 small steps of compression, the strain–stress response still appeared linear, as shown in Fig. 3(e). We quantified the relative compliance by fitting the two data sets to linear functions. The compliance ratio between the two states was estimated to be 0.67, which is close to the ratio of 0.64 measured in the standard compression test.

Figures 4(a)-4(f) show B-scan photoacoustic images of a cross section of the large blood vessel phantom before and after two large steps of compression with a step size of 500 μm, during which the strain reached the apparent nonlinear stress-

Downloaded From: https://www.spiedigitallibrary.org/conference-proceedings-of-spie on 9/4/2018
Terms of Use: https://www.spiedigitallibrary.org/terms-of-use

strain response regime. The blood vessel phantom became harder to compress in the presence of simulated thrombosis [Figs. 4(d)-d(f)], akin to the linear stress-strain response result. The strain values at the first compression state for the blood vessel phantom with and without simulated thrombosis were 12.9% ± 1.3% and 16.3% ± 1.1%, respectively. At the second compression state, they were 15.8% ± 1.4% and 22.4% ± 1.7%, respectively. Since the same compression stress was applied to the blood vessel phantom with and without simulated thrombosis at each state, the smaller strains indicated that a decrease in compliance of the blood vessel phantom was induced by the simulated thrombosis.

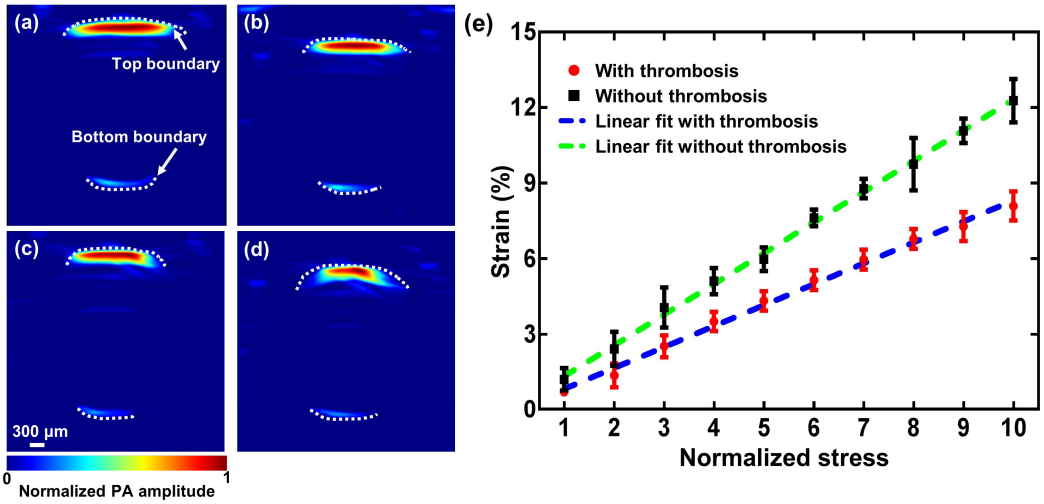

Figure 3. VE-PAT of a large blood vessel phantom in the linear stress-strain response regime. Photoacoustic images of a cross section in the large blood vessel phantom without simulated thrombosis (a) before and (b) after 10 small steps of compression and with simulated thrombosis (c) before and (d) after 10 small steps of compression. (e) Strain curves in 10 steps of compression for the large blood vessel phantom with and without simulated thrombosis. Dashed lines: linear fits with the coefficient of determination (R^2) of 0.998 and 0.995. Error bars: standard deviation.

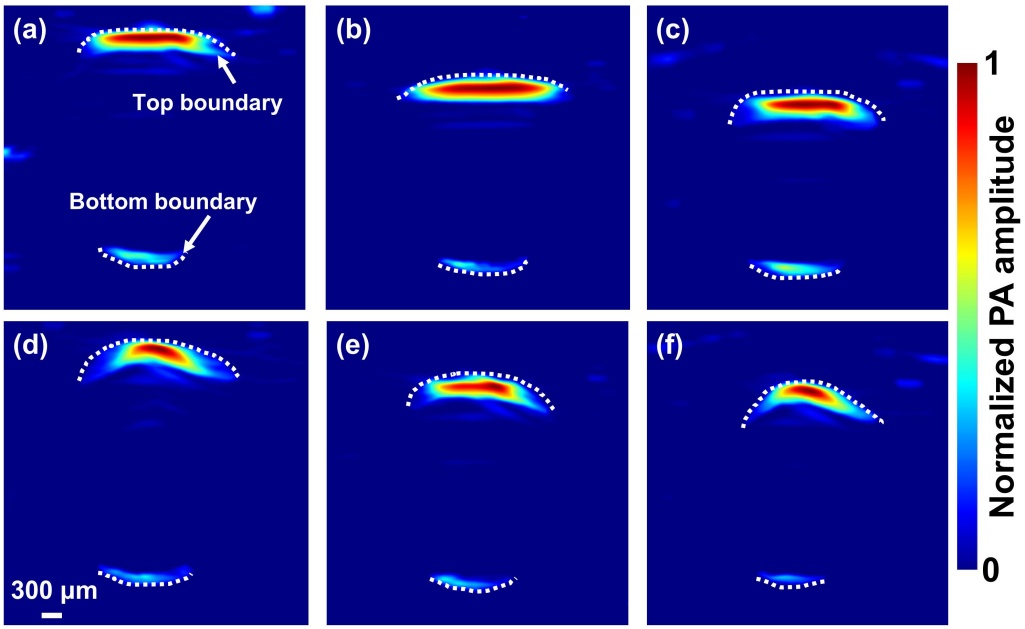

Figure 4. VE-PAT of a large blood vessel phantom in the nonlinear stress-strain response regime. Photoacoustic images of a cross section in the large blood vessel phantom without simulated thrombosis (a) before, (b) after one step of compression, and (c) after two steps of compression. Photoacoustic images of a cross section in the large blood vessel phantom with simulated thrombosis (d) before, (e) after one step of compression, and (f) after two steps of compression.

Downloaded From: https://www.spiedigitallibrary.org/conference-proceedings-of-spie on 9/4/2018
Terms of Use: https://www.spiedigitallibrary.org/terms-of-use

3.3 Vascular elastic photoacoustic tomography of small blood vessel phantom

Photoacoustic images of a cross section of the small blood vessel were acquired before and after compression with and without simulated thrombosis [Figs. 5(a)-5(d)]. Similar to the large blood vessel phantom, the small blood vessel phantom was harder to compress with the simulated thrombosis. The strain for the small blood vessel phantom without simulated thrombosis was 13.3% ± 0.9% while the strain with simulated thrombosis was only 6.7% ± 0.4%. Under the same compression stress, the decrease in strain indicated a decrease in compliance due to the simulated thrombosis.

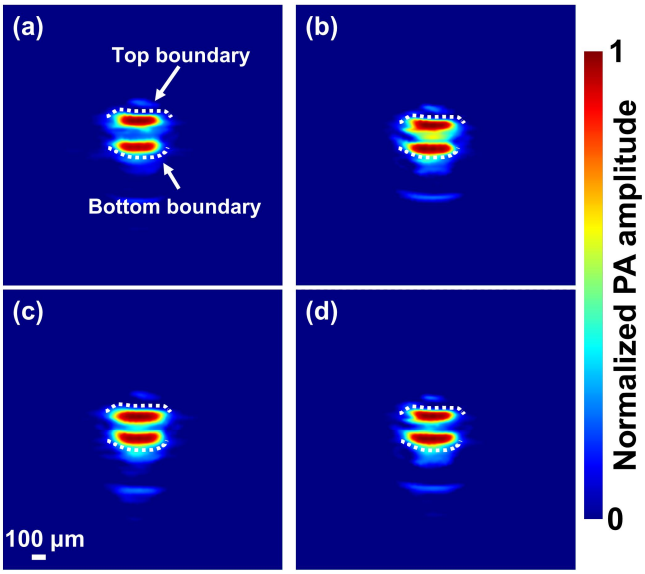

Figure 5. VE-PAT of a small blood vessel phantom. Photoacoustic images of a cross section in the small blood vessel phantom without simulated thrombosis (a) before and (b) after compression and with thrombosis (c) before and (d) after compression.

3.4 Vascular elastic photoacoustic tomography of blood vessels in a human

Figure 6 shows the VE-PAT results of the middle finger blood vessels of the human subject with and without vessel occlusion. During five small steps of compression with a step size of 50 μm, the blood vessel in the finger underwent smaller deformation with vessel occlusion downstream [Figs. 6(a)-6(d)]. Strain values for the blood vessels at each step of compression were calculated for both normal and vessel occlusion conditions [Fig. 6(e)]. Since the largest deformation was still within the linear stress-strain response regime, we estimated a relative decrease of compliance as 30.0% when the vessel was occluded.

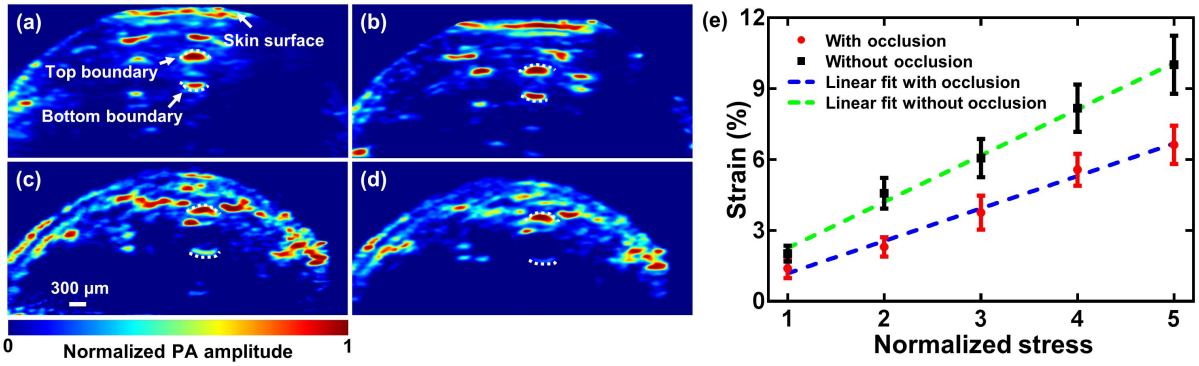

Figure 6. VE-PAT a human finger in the linear stress-strain response regime. Photoacoustic images of a cross section of the human finger without vessel occlusion (a) before and (b) after compression and with vessel occlusion (c) before and (d) after compression. (e) Strain curves under five steps of compression for the human finger with and without vessel occlusion. Dashed lines: linear fits with the coefficient of determination (R2) of 0.993 and 0.987. Error bars: standard deviation.

Downloaded From: https://www.spiedigitallibrary.org/conference-proceedings-of-spie on 9/4/2018
Terms of Use: https://www.spiedigitallibrary.org/terms-of-use

The finger was then compressed with two 300 μm steps, during which the blood vessels underwent larger deformation so that the stress-strain response became nonlinear [Figs. 7(a)-7(f)]. Again, the blood vessels with occlusion underwent smaller deformation than that without occlusion under the same load. Strain values for blood vessels without occlusion at the two steps were 37.5% ± 5.8% and 47.9% ± 6.1%, while they were 16.7% ± 3.4% and 22.9% ± 4.5% with vessel occlusion. These results demonstrated that VE-PAT can detect the decrease of vessel compliance in the human finger due to vessel occlusion in both the linear and nonlinear stress-strain response regimes.

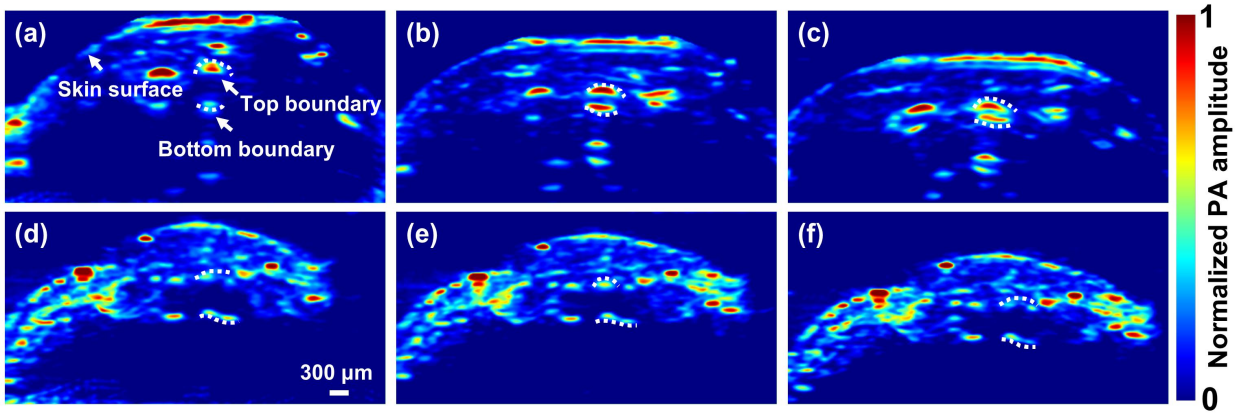

Figure 7. VE-PAT a human finger in the nonlinear stress-strain response regime. Photoacoustic images of a cross section of the human finger without vessel occlusion (a) before compression, (b) after compression step 1, and (c) after compression step 2. Photoacoustic images of the same cross section of the human finger with vessel occlusion (d) before compression, (e) after compression step 1, and (f) after compression step 2.

4. DISCUSSIONS AND CONCLUSIONS

By incorporating a linear-array-based photoacoustic imaging probe with a customized compression stage, we have developed VE-PAT that can detect blood vessel elasticity changes due to abnormal hemodynamic states. VE-PAT detected vascular compliance changes due to simulated thrombosis in large and small blood vessel phantoms at depths and in blood vessels in a finger of a human subject in vivo. In the large blood vessel phantom, the compliance ratio between the two states with and without simulated thrombosis measured by VE-PAT agreed with the value measured in the standard compression test. By imaging the small blood vessel phantom embedded 3 mm deep in the gelatin phantom, VE-PAT demonstrated its capability to detect elasticity changes of small blood vessels at depths that are difficult for either USE or OCE to image. In addition, VE-PAT was applied to assess blood vessel elasticity changes due to vessel occlusion in the human finger, demonstrating its potential for clinical vessel elasticity characterization.

The detection sensitivity of the VE-PAT system is limited by the minimum detectable displacement, that is, 18.3 μm. First, the minimum detectable displacement limits the minimum diameter of blood vessels whose elasticity can be assessed by VE-PAT in the linear strain–stress response regime, which is usually considered to be less than 10% strain in biological tissue. To stay within the linear strain–stress response regime, the blood vessel diameter should be at least 183 μm, that is, 10 times (reciprocal of 10%) the minimum detectable displacement. For blood vessels with diameters smaller than 183 μm and larger than the minimum detectable displacement of 18.3 μm, their elasticity can still be assessed, but only in the nonlinear stress–strain response regime. For blood vessels with diameters smaller than 18.3 μm, their deformation cannot be resolved, which is the ultimate detection limit of the current VE-PAT system.

To the best of our knowledge, this is the first time that PAT has been applied for quantitative assessment of blood vessel elastic properties in humans in vivo. In addition to the information that photoacoustic imaging can provide including structure, flow velocity, molecule concentration, and oxygen saturation level of hemoglobin, VE-PAT adds important elasticity information[27-29]. VE-PAT has potential for use in many clinical applications, including detection of deep venous thrombosis, characterization of vulnerable plaque, and evaluation of atherosclerotic tissues.

Downloaded From: https://www.spiedigitallibrary.org/conference-proceedings-of-spie on 9/4/2018
Terms of Use: https://www.spiedigitallibrary.org/terms-of-use

ACKNOWLEDGMENTS

We thank Alejandro Garcia-Uribe for his assistance in human experiments and Professor James Ballard for a close reading of this paper. This work was sponsored by the National Institutes of Health Grants DP1 EB016986 (NIH Director's Pioneer Award), R01 CA186567 (NIH Director's Transformative Research Award), and S10 RR026922. L. V. Wang has a financial interest in Endra, Inc., and Microphotoacoustics, Inc., which, however, did not support this work.

REFERENCES

[1] Greenleaf, J.F., Fatemi, M. and Insana, M., "Selected methods for imaging elastic properties of biological tissues," Annu. Rev. Biomed. Eng. 5(1), 57-78 (2003).
[2] Gao, L., Parker, K.J., Lerner, R.M. and Levinson, S.F., "Imaging of elastic properties of tissue-a review," Ultrasound Med. Biol. 22 (8), 959–977 (1996).
[3] Pasterkamp, C. and Falk, E., "Atherosclerotic plaque rupture: an overview," J Clin Basic Cardiol. 3(2), 81-86 (2000).
[4] Emelianov, S.Y., Chen, X., O'Donnell, M., Knipp, B., Myers, D., Wakefield, T.W. and Rubin, J.M., "Triplex ultrasound: elasticity imaging to age deep venous thrombosis," Ultrasound Med. Biol. 28(6), 757–767 (2002).
[5] Ophir, J., Cespedes, I., Ponnekanti, H., Yazdi, Y. and Li, X., "Elastography: a quantitative method for imaging the elasticity of biological tissues," Ultrasonic imaging, 13(2), 111-134 (1991).
[6] Ophir, J., Alam, S.K., Garra, B.S., Kallel, F., Konofagou, E.E., Krouskop, T., Merritt, C.R., Righetti, R., Souchon, R., Srinivasan, S. and Varghese, T., "Elastography: Imaging the elastic properties of soft tissues with ultrasound," Journal of Medical Ultrasonics, 29(4), 155-171 (2002).
[7] Manduca, A., Oliphant, T.E., Dresner, M.A., Mahowald, J.L., Kruse, S.A., Amromin, E., Felmlee, J.P., Greenleaf, J.F. and Ehman, R.L., "Magnetic resonance elastography: non-invasive mapping of tissue elasticity," Medical Image Analysis 5(4), 237-54 (2001).
[8] Sun, C., Standish, B., and Yang, V. X. D., "Optical coherence elastography: current status and future applications," J. Biomed. Opt., 16(4), 043001 (2011).
[9] Hai, P., Yao, J., Li, G., Li, C., and Wang, L. V., "Photoacoustic elastography," Opt. Lett. 41(4), 725-728 (2016).
[10] De Korte, C.L. and Van Der Steen, A.F., "Intravascular ultrasound elastography: an overview," Ultrasonics 40(1), 859-865 (2002).
[11] De Korte, C.L., van der Steen, A.F., Céspedes, E.I., Pasterkamp, G., Carlier, S.G., Mastik, F., Schoneveld, A.H., Serruys, P.W. and Bom, N., "Characterization of plaque components and vulnerability with intravascular ultrasound elastography," Phys. Med. Biol. 45(6), 1465–1475 (2000).
[12] Schmitt, C., Soulez, G., Maurice, R.L., Giroux, M.F. and Cloutier, G., "Noninvasive Vascular Elastography: Toward A Complementary Characterization Tool of Atherosclerosis in Carotid Arteries," Ultrasound Med. Biol. 33(12), 1841–1858 (2007).
[13] Woodrum, D.A., Herrmann, J., Lerman, A., Romano, A.J., Lerman, L.O. and Ehman, R.L., "Phase-contrast MRI-based elastography technique detects early hypertensive changes in ex vivo porcine aortic wall," J Magn Reson Imaging 29(3), 583–587 (2010).
[14] Rogowska, J., Patel, N., Plummer, S. and Brezinski, M.E., "Quantitative optical coherence tomographic elastography: Method for assessing arterial mechanical properties," Br. J. Radiol. 79(945), 707–711 (2006).
[15] Wang, L.V. and Hu, S., "Photoacoustic tomography: in vivo imaging from organelles to organs," Science 335(6075), 1458-1462 (2012).
[16] Hai, P., Yao, J., Maslov, K. I., Huang, C., and Wang, L. V., "Photoacoustic microscopy of epilepsy in mouse brain with high spatial-temporal resolution," Scientific reports (under review).
[17] Liang, J., Gao, L., Li, C. and Wang, L.V., "Spatially Fourier-encoded photoacoustic microscopy using a digital micromirror device," Opt. Lett. 39(3), 430 (2014).
[18] Yeh, C., Hu, S., Maslov, K. and Wang, L.V., "Photoacoustic microscopy of blood pulse wave," J. Biomed. Opt. 17(7), 070504 (2012).
[19] Hai, P., Zhou, Y., Liang, J., Li, C. and Wang, L.V., "Photoacoustic tomography of vascular compliance in humans," J. Biomed. Opt. 20(12), 126008 (2015).
[20] Gao, G., Yang, S. and Xing, D., "Viscoelasticity imaging of biological tissues with phase-resolved photoacoustic measurement," Opt. Lett. 36(17), 3341–3343 (2011).

Downloaded From: https://www.spiedigitallibrary.org/conference-proceedings-of-spie on 9/4/2018
Terms of Use: https://www.spiedigitallibrary.org/terms-of-use

[21] Needles, A., Heinmiller, A., Sun, J., Theodoropoulos, C., Bates, D., Hirson, D., Yin, M. and Foster, F.S., "Development and initial application of a fully integrated photoacoustic micro-ultrasound system," IEEE Trans. Ultrason. Ferroelectr. Freq. Control 60(5), 888–897 (2013).
[22] Zhou, Y., Liang, J. and Wang, L.V., "Cuffing-based photoacoustic flowmetry in humans in the optical diffusive regime," J. Biophotonics, 1(5) (2015).
[23] Xu, M., and Wang, L. V., "Universal back-projection algorithm for photoacoustic computed tomography," Phys. Rev. E. 71(1), 016706 (2005).
[24] Hall, T.J., Bilgen, M., Insana, M.F. and Krouskop, T.A., "Phantom materials for elastography," IEEE Trans. Ultrason. Ferroelectr. Freq. Control 44(6), 1355–1365 (1997).
[25] Hai, P., Zhou, Y., Gong, L., and Wang, L.V., "Quantitative photoacoustic elastography in humans," Optica (under review).
[26] Kennedy, B.F., Hillman, T.R., McLaughlin, R.A., Quirk, B.C. and Sampson, D.D., "In vivo dynamic optical coherence elastography using a ring actuator," Opt. Express 17(24), 21762–21772 (2009).
[27] Hai, P., Yao, J., Maslov, K.I., Zhou, Y. and Wang, L.V., "Near-infrared optical-resolution photoacoustic microscopy," Opt. Lett. 39(17), 5192-5195 (2014).
[28] Liang, J., Zhou, Y., Maslov, K.I. and Wang, L.V., "Cross-correlation-based transverse flow measurements using optical resolution photoacoustic microscopy with a digital micromirror device," J. Biomed. Opt., 18(9), 096004 (2015).
[29] Zhang, H.F., Maslov, K., Stoica, G. and Wang, L.V., "Functional photoacoustic microscopy for high-resolution and noninvasive in vivo imaging," Nat. Biotechnol. 24 (7), 848-851 (2006).

Downloaded From: https://www.spiedigitallibrary.org/conference-proceedings-of-spie on 9/4/2018
Terms of Use: https://www.spiedigitallibrary.org/terms-of-use